The Astronomical Journal, 137:246–256, 2009 January doi:10.1088/0004-6256/137/1/246

THE ACS SURVEY OF GALACTIC GLOBULAR CLUSTERS. VI. NGC 6366: A HEAVILY STRIPPED GALACTIC GLOBULAR CLUSTER*

Nathaniel E. Q. Paust[1], Antonio Aparicio[2], Giampaolo Piotto[3], I. Neill Reid[1], Jay Anderson[1], Ata Sarajedini[4], Luigi R. Bedin[1], Brian Chaboyer[5], Aaron Dotter[5], Maren Hempel[4], Steven Majewski[6], A. Marín-Franch[7], Antonino Milone[8], Alfred Rosenberg[7], and Michael Siegel[9]

[1] Space Telescope Science Institute, 3700 San Martin Drive, Baltimore, MD 21218, USA; npaust@stsci.edu, inr@stsci.edu, anderson@stsci.edu, bedin@stsci.edu
[2] Department of Astrophysics, University of La Laguna and Instituto de Astrofísica de Canarias, Vía Láctea s/n, E-38200 La Laguna, Spain; antapaj@iac.es
[3] Dipartimento di Astronomia, University di Padova, vicolo dell'Osservatorio 5, I-35122 Padova, Italy; piotto@pd.astro.it
[4] Department of Astronomy, University of Florida, 211 Bryant Space Science Center, Gainesville, FL 32611, USA; ata@astro.ufl.edu, hempel@astro.ufl.edu
[5] Department of Physics and Astronomy, Dartmouth College, 6127 Wilder Laboratory, Hanover, NH 03755, USA; chaboyer@heather.dartmouth.edu, dotter@uvic.ca
[6] Department of Astronomy, University of Virginia, P.O. Box 400325, Charlottesville, VA 22904-4325, USA; srm4n@virginia.edu
[7] Instituto de Astrofísica de Canarias, Vía Láctea s/n, E-38200 La Laguna, Spain; amarin@iac.es, alf@iac.es
[8] Dipartimento di Astronomia, Università di Padova, Vicolo dell' Osservatorio 3, Padova, I-35122, Italy; milone@pd.astro.it
[9] University of Texas, McDonald Observatory, 1 University Station, C1402, Austin, TX 78712, USA; siegel@astro.as.utexas.edu

Received 2008 February 29; accepted 2008 October 1; published 2008 December 15

ABSTRACT

We have used observations obtained as part of the *Hubble Space Telescope*/ACS Survey of Galactic globular clusters (GCs) to construct a color–magnitude diagram for the bulge cluster, NGC 6366. The luminosity function derived from those data extends to $M_{F606W} \sim 9$, or masses of $\sim 0.3\,M_{\odot}$. Unlike most GCs, the mass function peaks near the main-sequence turnoff with significantly fewer low-mass stars even after correction for completeness and mass segregation. Using a multimass King model, we extrapolate the global cluster behavior and find the global mass function to be poorly matched by a power law, with a particular deficit of stars with masses between 0.5 and $0.7\,M_{\odot}$. We briefly discuss this interesting anomaly within the context of tidal stripping.

Key words: galaxies: luminosity function, mass function – globular clusters: general – globular clusters: individual (NGC 6366)

1. INTRODUCTION

Galactic globular clusters (GCs) have been considered as the ideal laboratories for the study of the complex interplay between stellar dynamics and stellar evolution. In recent years, the availability of ground-based wide-field imaging facilities and the *Hubble Space Telescope* (*HST*) have made it possible to cover all the evolutionary sequences in GCs, from the cluster centers to the outskirts. The high angular resolution of *HST* offers particular advantages in crowded regions, and initial observations are concentrated on cluster cores (e.g. De Marchi & Paresce 1994). With the installation of WFPC2, more panoramic studies became possible, including luminosity function determinations for 47 Tucanae (De Marchi & Paresce 1995), NGC 2419 and M92 (Harris et al. 1997), M4 (Richer et al. 1997), and NGC 6397 (King et al. 1998), while Piotto et al. (2002) undertook a SNAPSHOT Survey of 74 GCs. Many of these observations, however, reach only 1–2 mag below the main-sequence turnoff (MSTO).

The installation of the Advanced Camera for Surveys (ACS) in Servicing Mission 3B provided *HST* with greater sensitivity and increased areal coverage, permitting investigations of the cool subdwarf and white dwarf sequences in the nearest clusters. In particular, concentrated campaigns have produced data that reach the hydrogen-burning limit in closer clusters such as NGC 6397 (Richer et al. 2008) and M4 (Bedin et al. 2001; Richer et al. 2002). The *HST* data accumulated in these investigations have been used to probe the luminosity functions and mass functions to various depths in a number of clusters. In general, the results are characterized either as a log–normal distribution, with a characteristic mass $\sim 0.33\,M_{\odot}$ (Paresce & De Marchi 2000), or as a power-law distribution, $dN/dM = m^{\alpha}$, with indices $\alpha \sim -1$ (Piotto & Zoccali 1999). In either case, the overall form of the mass function is broadly consistent with analyses of observations of lower-mass stars in the Solar Neighborhood (Reid et al. 2002). We are currently using the data obtained in the course of the ACS Galactic Globular Cluster Survey (ACS GGC; Sarajedini et al. 2007) to determine mass functions extending to $\sim 0.2 M_{\odot}$ for 65 clusters. We will discuss the bulk of those results, and correlations between the parameterized mass function and other intrinsic properties, in a future paper; here, we present our analysis of NGC 6366, one of the more unusual clusters in the sample.

GCs provide insight into how dynamical effects can lead to the dissipation of star clusters. Over time, the radial distribution of stars in the cluster is governed by relaxation processes (Spitzer 1987) that allow high-mass objects to settle in the cluster core and throw low-mass stars to the periphery of the cluster where tidal stripping and shocks can remove them from the cluster. These effects lead to significant evolution in the cluster luminosity function. Indeed, while all indications are that the star-formation process favors lower masses, with low-mass stars greatly outnumbering high-mass stars, several clusters including NGC 2298 (De Marchi & Pulone 2007), NGC 6218 (De Marchi et al. 2006), NGC 6712 (De Marchi et al. 1999; Andreuzzi et al. 2001), and Pal 5 (Koch et al. 2004) have present-day mass functions (PDMFs) which are either flat or have indices $\alpha > 0$.

Many of the tidally stripped clusters are denizens of the Galactic bulge, and are therefore subject to relatively frequent passages through high-density central regions of the Milky Way. NGC 6366 is one of the less-studied members of the bulge

* Based on observations made with the NASA/ESA *Hubble Space Telescope*, obtained at the Space Telescope Science Institute, which is operated by the Association of Universities for Research in Astronomy, Inc., under NASA contract NAS 5-26555. These observations are associated with program GO-10775.

population with extremely limited ground-based observations making up the only previous studies. Consequently, the published photometry barely reaches 2 mag below the MSTO in the color–magnitude diagram (CMD) and we have no direct information on the orbital characteristics.

In this paper we present analysis of new observations of NGC 6366 using the ACS Wide Field Channel (ACS/WFC). We find that the global PDMF for this cluster shows a steep slope (declining numbers with decreasing mass) and a very interesting non–power-law shape. Section 2 describes the observations, photometry, and data analysis. Section 3 discusses dynamical models of the cluster and reveals the cluster mass function. Our conclusions are given in Section 4.

2. OBSERVATIONS, PHOTOMETRY, AND DATA ANALYSIS

2.1. Color–Magnitude Diagram

NGC 6366 was observed using the ACS/WFC as part of the *HST* treasury program "An ACS Survey of Galactic Globular Clusters" (GO 10775 P.I. Ata Sarajedini). A total of 10 exposures were made with four 140 s "long" exposures and a single 10 s "short" exposure in the F606W and F814W filters. As with all of the clusters in this program, the observations were centered on the cluster core. NGC 6366 lies at $\alpha = 17^{\rm h}27^{\rm m}44^{\rm s}$, $\delta = -5°4'36''$, or Galactic latitude $b = +16°$, longitude $l = +18°$. The cluster has a core radius of 1′.57 and the ACS observations cover an area 3′.3 × 3′.3 in size.

Previous investigations of NGC 6366 include a photographic study by Pike (1976) to a depth slightly below the horizontal branch. Harris (1993) obtained deeper ground-based observations, aimed primarily at exploring the blue straggler and variable star population of the cluster. More recently, Alonso et al. (1997) obtained ground-based BV photometry that extends to $V \sim 20.5$, or ∼1.5 mag below the turnoff. Based on those data, they estimate a foreground reddening of $E(B-V) = 0.70$ mag from which a distance modulus was derived of $(m-M)_\circ = 12.26$ mag, or $d \sim 2.8$ kpc. This corresponds to a Galactocentric radius of $R_{\rm GC} = 4.9$ kpc (Rosenberg et al. 2000).

For this study, stellar magnitudes were measured in the ACS images using the ePSF method of Anderson & King (2006). A full description of the measurements and photometric analysis is given in Anderson et al. (2008). In our procedure, we measure the stars directly on the *HST* `flt` images in order to determine the best possible flux and position for each star. While drizzled images are often used in photometry, the drizzling process distorts the point-spread function, resulting in significantly poorer photometry in crowded regions. The CMD derived from our analysis is shown in Figure 1. It is clear that NGC 6366 has modest populations of equal-mass main-sequence binaries (a fractional contribution of ∼5% on the upper main sequence) and blue stragglers. We discuss the spatial distribution of those stars in the following section.

Isochrone fitting using isochrones from the Dartmouth Stellar Evolution Program (DSEP; Dotter et al. 2007) was used to determine the distance modulus and reddening of the cluster, a task complicated by the wide range of metallicities quoted for NGC 6366 in the literature. Zinn & West (1984) give [Fe/H] = −0.99 ± 0.25 based on narrowband photometry. Carretta & Gratton (1997) recalibrated the Zinn & West measurements using their high-resolution spectroscopy of red giants in 24 clusters, and adopting their scale gives an abundance of [Fe/H] = −0.73 for NGC 6366. Finally, De Angeli et al. (2005) apply their own rescaling of the Zinn & West abundances to derive [Fe/H] = −0.58. Our analysis shows that the observed CMD is best fit by an isochrone at the lower end of the metallicity range, so the Zinn & West (1984) abundance was adopted as a starting point. This work uses scaled-solar metallicity isochrones so an adjustment was required based on the assumed α-element enhancement of the cluster. Assuming [α/Fe] = 0.2 and using the result presented by Salaris et al. (1993), the overall metal abundance is $Z = Z_0(0.638\,f_\alpha + 0.362)$ where Z_0 is the iron abundance and f_α is the α-element enhancement. This corresponds to a scaled solar metallicity of [Fe/H] = −0.85. Consequently, isochrones with [M/H] = −0.70, −0.85, and −1.10 generated in the native *HST* filter system were matched against the cluster. This can be seen in Figure 1. All of the isochrones shown are 13.5 Gyr old with the distance modulus and color excess shifted to best match the CMD. The scaled-solar [Fe/H] = −0.85 models for age 13.5 Gyr give the best fit, and we adopt these as the reference set in this paper.

Matching against the 13.5 Gyr isochrone, we find a color excess of $E(\text{F606W}-\text{F814W}) = 0.76$ and an apparent distance

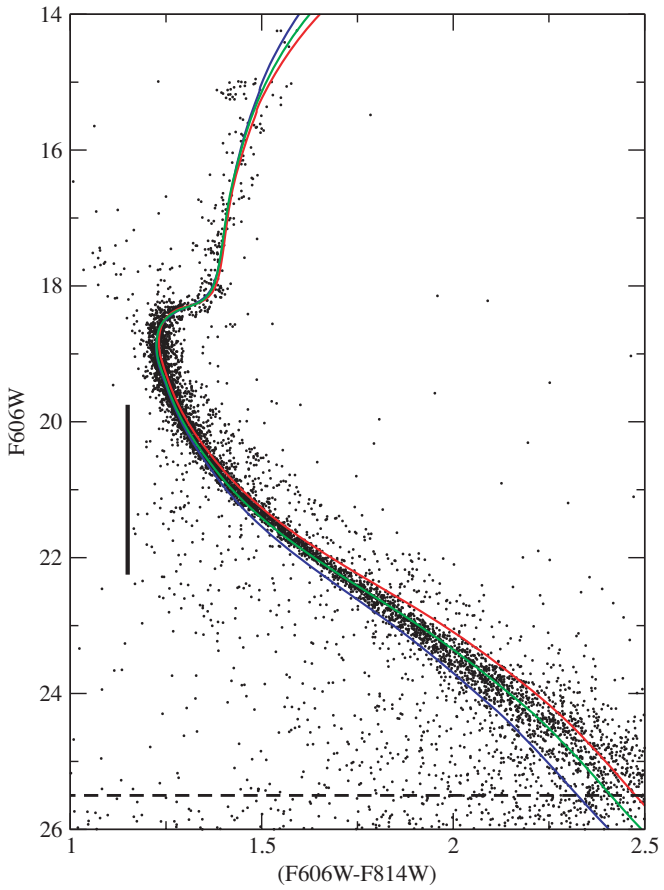

Figure 1. CMD of NGC 6366. A 13.5 Gyr isochrone with [Fe/H] = −0.85 from Dotter et al. (2007) is shown in green with the CMD. A color excess of $E(\text{F606W}-\text{F814W}) = 0.76$ and a distance modulus of $(m-M)_{\text{F606W}} = 14.8$ were used to match isochrone and observations. The red line is a 13.5 Gyr [Fe/H] = −0.70 isochrone with $(m-M)_{\text{F606W}} = 14.7$ and $E(\text{F606W}-\text{F814W}) = 0.74$ which is systematically too red along the main sequence. The blue line is a 13.5 Gyr [Fe/H] = −1.10 isochrone with $(m-M)_{\text{F606W}} = 14.8$ and $E(\text{F606W}-\text{F814W}) = 0.78$ showing a systematic blue offset. The distance modulus and color excess for the high and low metallicity lines have been adjusted to best match the CMD and are extremely close to the values used for the [Fe/H] = −0.85 line. The solid black vertical line shows the magnitude range corresponding to the dip in the global PDMF. The horizontal dashed line shows the $m_{\text{F606W}} = 25.5$ mag limit adopted for the mass function.

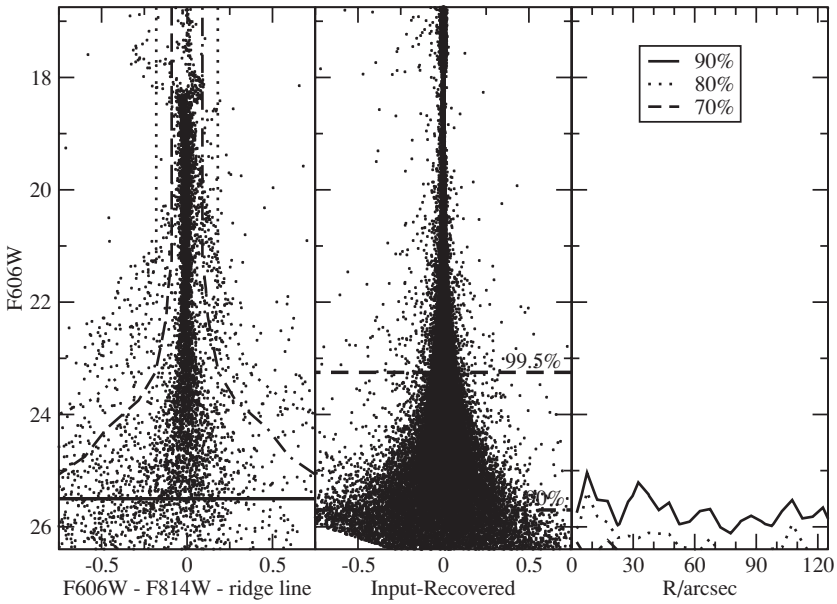

Figure 2. Examination of the NGC 6366 CMD and completeness. The leftmost panel shows the CMD of NGC 6366 with ridge color subtracted. The dashed and dotted lines are, respectively, the 3σ and 6σ limits used to separate cluster and field stars. The solid horizontal line at $m_{F606W} = 25.5$ shows the magnitude limit for our adopted sample. The center panel shows the recovered artificial star distribution with the completeness as a function of magnitude in the input 25″–50″ annulus. The right panel is a contour map showing completeness as a function of magnitude and cluster radius. Due to the lack of crowding in the cluster, the contour map is very sparse and the majority of the cluster is complete at over the 90% level dropping to 80% a half magnitude below our region of interest.

modulus of $(m - M)_{F606W} = 14.8$. Using the relation found in Bedin et al. (2005), the average reddening for the cluster results in an extinction of $A_{F606W} = 2.20$ and an extinction-corrected distance modulus of $(m - M)_\circ = 12.6$. We have applied no corrections for differential reddening across the cluster. Even though the extinction is rather high, the broadening of the main sequence is rather small. We feel that such a small broadening will have a minimal effect on the mass function derived here.

2.2. Completeness and Field Star Contamination

After identifying all the stars in the ACS images, we ran artificial star tests using 10^5 artificial stars to assess the completeness and measurement quality for the data set. The artificial stars were analyzed using the method outlined in Paust et al. (2007) to determine completeness as a function of both magnitude and distance from the cluster center. The input and recovered artificial stars are binned on an annular grid with a radial spacing of 100 pixels (5″) and 0.5 mag sampling in luminosity. The ratio of recovered-to-input artificial stars in each bin gives the completeness. In this process, all objects with photometric uncertainties greater than 0.4 mag in F606W or F814W were removed from the photometric catalog, with similar cuts applied to the artificial star catalog. Background galaxies are not well fit by the stellar point-spread function resulting in larger photometric errors resulting in their removal from the catalog after clipping by photometric uncertainty. The artificial stars are added with realistic Poisson noise and are measured using the same procedure used for the real stars. The measured artificial stars must be within ±0.75 pixels of the input position and within ±0.75 mag of the input magnitude. This greatly reduces false-positive detections where a real star might be counted as a recovered artificial star. Over the magnitude range of interest for this paper from roughly the MSTO down to $m_{F606W} = 25.5$, the input and recovered magnitudes of the artificial stars differ by an amount less than the 3σ limits used to separate cluster and field stars. This consistent choice assures that the artificial stars are not held to a higher standard than the real stars and ensures that the artificial stars follow the same trends in completeness as the real stars. To determine completeness the ratio of recovered to input artificial stars is examined as a function of cluster radius and magnitude. NGC 6366 is a fairly sparse cluster with a low degree of crowding resulting in very high completeness. The right panel of Figure 2 illustrates that the photometry is better than 90% complete over the magnitude and radius range used to determine the stellar mass function. This map of completeness in radius and magnitude is then interpolated to weight the real stars when binned in the luminosity function or mass function.

The artificial star tests show that our photometric data reach the 50% completeness level at approximately $m_{F606W} = 26.75$ independent of the radius since crowding is minimal in the cluster. However, due to increasing field star contamination at faint magnitudes and a scarcity of cluster stars, this work deals only with photometry to $m_{F606W} = 25.5$ where the stellar sample is better than 90% complete. As in Paust et al. (2007), a σ-clipping routine was used to remove field stars and stars not on the main sequence, subgiant branch, and red giant branch sequences. This method will result in the elimination of some equal-mass binary cluster members, and will not remove field stars that lie along the cluster sequences. However, those stars do not have a large effect (<10%) on the luminosity function or mass function for the cluster.

Field star contamination can be easily seen and quantified with a ridge-color-subtracted CMD following the method outlined in Cool et al. (1996). This diagram can be seen in Figure 2, and we can use these data to derive a reliable estimate of the number of field stars contaminating the NGC 6366 luminosity function. In the figure, the dashed lines are shown at $\pm 3\sigma$ from the ridge and the dotted lines are at $\pm 6\sigma$, where σ is the average photometric error at a given magnitude. The number of stars between the two sets of lines should be approximately equal to the number of contaminating field stars in the

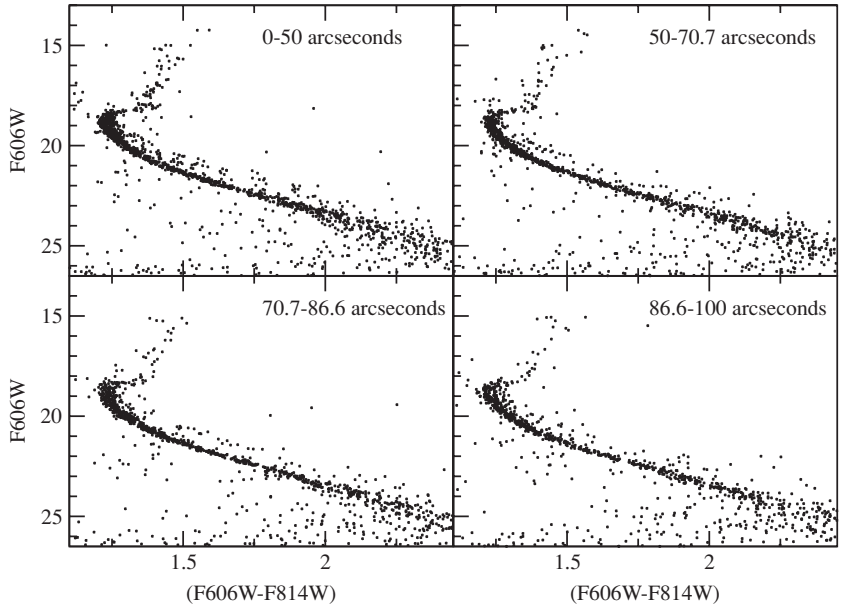

Figure 3. CMDs for four equal-area regions centered on NGC 6366, covering radii from 0″ to 50″, 50″ to 70.″7, 70.″7 to 86.″6, and 86.″6 to 100″. As discussed in the text, the inner CMDs include significant numbers of main-sequence binaries and blue stragglers.

main-sequence region. Considering the annulus from 25″ to 50″, the region taken as the reference for the multimass King models discussed in Section 3, there are between 0 and 10 contaminating field stars per magnitude to the $m_{F606W} = 25.5$ cutoff. Figure 2 shows that the statistical subtraction eliminates a similar number of equal-mass binaries. In comparison, there are between 100 and 170 cluster members per magnitude. Field star contamination is therefore a small issue, at worst 5%, in the luminosity function and mass function. Moreover, the field star population increases in number with decreasing magnitude (Figures 1 and 2). Consequently, any significant contamination should lead to an overestimate of the number of cluster members at low masses and to an inferred mass function that is too steep (too negative a slope). In contrast, as will be discussed in Section 3.3, the mass function that we infer for NGC 6366 is flatter (more positive index) than the results measured for most other clusters; thus, subtracting additional stars for field contamination can only make the derived mass function more positive.

We will consider dynamical evolutionary effects in more detail in the following section. However, Figure 3 provides a qualitative illustration of mass segregation in NGC 6366. We have divided the ACS data set into four equal areas, covering radii from 0″ to 50″, 50″ to 70.″7, 70.″7 to 86.″6, and 86.″6 to 100″. Figure 3 shows the CMDs for each region. Since each segment covers an equal area, the field star contribution should be statistically the same in each. We note that both the binaries and the blue stragglers are concentrated toward the central regions of the cluster, as one would expect for higher-mass objects. Even in the center, however, the relative number of stars on the photometric binary sequence is only ∼10% of normal main-sequence stars (A. Milone et al. 2008, in preparation). We have not attempted to deconvolve the photometric binaries and include those stars in the luminosity function calculations described in the following section. The likely properties of both binaries and blue stragglers will be discussed in more detail in a future paper that will consider the broader context of binary populations in the full ACS GGC Survey.

3. DYNAMICAL MODELS AND THE MASS FUNCTION

3.1. Methodology

The ACS/WFC covers a field of view of approximately 202″ × 202″, and our observations therefore include only the central regions of the clusters targeted by the ACS GCC Survey. Theoretical models (e.g. Spitzer 1987) predict that energy equipartition should lead to mass segregation. This was first observed by Sandage (1954) in M3 and Tayler (1954) in M92 although the mass segregation was mentioned only in passing. Oort & van Herk (1959) expanded on the data from Sandage and gave the first clear demonstration of mass segregation. More recently, mass segregation was observed in 47 Tucanae by Da Costa (1982) using ground-based observations and by Paresce et al. (1995) using *HST*. Further early *HST* work (e.g. King et al. 1995) have confirmed the presence of mass segregation in other clusters. The ACS observations in this program are centered on the cluster, so mass segregation dictates that the luminosity function, and hence the mass function, measured directly from the data is biased toward more luminous, higher-mass stars. Dynamical models need to be employed to convert the observed quantities to parameters that characterize the global cluster properties. These adjustments need to be applied to all the ACS GGC observations, so we take this opportunity to outline the general techniques employed.

Our analysis uses the dynamical models developed by Anderson (1997), which are in turn based on the multicomponent King-model formalism developed by Gunn & Griffin (1979). The models are constrained to be isotropic and the cluster stars are partitioned into separate mass components by combining luminosity function data with an appropriate mass–luminosity relation (MLR). As discussed in more detail in Section 3.3, we use mass–luminosity data from DSEP models (Dotter et al. 2007). The formalism that we adopt is as follows.

1. We define the model mass components via the luminosity function, binning the stars in 1 mag intervals along the main sequence, with the characteristics mass of each bin and the mass limits for each bin set by the MLR for the appropriate metallicity. Stars from the tip of the red giant branch to

our completeness limits are included, encompassing red giant branch stars, stars on the horizontal branch, subgiants, blue stragglers, MSTO stars, and regular main-sequence stars. The model includes additional mass bins to represent compact objects in the form of $\sim 1.5\ M_{\odot}$ neutron stars and $\sim 0.6\ M_{\odot}$ white dwarfs.

2. The structural parameters (the core radius, r_c, and tidal radius, r_t) are constrained using the cluster surface-brightness profile. Integrating the luminosity function of a typical GC shows that the light profile is dominated by evolved stars, with $\sim$85% of the total flux coming from stars brighter than the MSTO. The cluster luminosity profile therefore constrains the spatial distribution of stars with mass $\sim 0.8\ M_{\odot}$.
3. The mass distribution within a reference region at a particular radius is constrained by measuring the luminosity function within an annulus. The sampling region needs to be sufficiently wide to ensure both sufficient numbers of stars for reliable statistics, but sufficiently narrow to minimize differential mass segregation.

Given these initial constraints, the models are used to generate the predicted radial distributions of each mass component. Those predictions are verified by matching the predicted luminosity function against the measured results at a range of radii. Note that the model predicts both the shape of the luminosity function and the normalization as a function of radius; that is, there are no free parameters in matching against the data. The final outcome is a weighting function that scales the observed luminosity function in the reference region to give a luminosity function that represents the integrated cluster properties, the global luminosity function.

3.2. The Global Luminosity Function of NGC 6366

We have applied the techniques outlined in Section 3.1 in our analysis of NGC 6366. The reference region for the luminosity function is defined as an annulus with inner radius 25″ from the cluster center and an outer radius of 50″. This gives a reference sample of approximately 1000 stars. In comparison, there are approximately 590 stars inside 25″, slightly more than 2400 stars in the annulus between 50″ and 75″, and just over 4000 stars in the outer annulus from 75″ to 110″. The luminosity functions measured in these other regions serve as constraints on the derived multi-component mass model.

NGC 6366 is a Bulge cluster, and has experienced extensive dynamical interactions over its lifetime. As discussed further below, those interactions appear to have resulted in significant mass stripping and the preferential removal of lower-mass main-sequence stars. This has implications for the contribution of (relatively high mass) degenerate remnants to the total mass budget. Consider an initial mass function (IMF) comparable with the local Galactic disk; that distribution can be represented as a composite power law, with index $\alpha = -1$ for stars below $1\ M_{\odot}$ and $\alpha = -2.3$ at higher masses. If we assume a turnoff mass of $0.8\ M_{\odot}$, and assume that stars with $M > 6.5\ M_{\odot}$ have evolved to neutron star remnants, then we expect $\sim$15% of the initial stellar population to have evolved to white dwarfs, while $\sim$0.5% are neutron stars. As lower-mass main-sequence stars are removed from the cluster, those fractions will increase. We have examined the effect of increasing these fractions by up to a factor of 10. Our tests indicate that the derived global mass function is affected at less than the 20% level, comparable with the overall uncertainty from other sources. Thus, changing the compact object fractions does not have a significant effect on our conclusions regarding the global mass function of this cluster.

Trager et al. (1995) derive a core radius of 1.′83 for NGC 6366, and Harris (1996) cites a half-mass radius of 2.′63 and a tidal radius of 15.′2. We have combined the ACS/WFC observations with the surface-brightness profile from Trager et al. (1995), converting the latter measurements to F606W magnitudes using the average color of stars above the MSTO and transformations from Sirianni et al. (2005). We derive revised values of 1.′57 for the core radius and 24.′2 for the tidal radius. The Trager et al. (1995) data extend to radii of only $\sim 9'$, so the latter parameter is weakly constrained by the surface-brightness profile. However, changes in the model tidal radius produce noticeable changes in the luminosity functions seen in Figure 4 resulting in a stronger constraint on the tidal radius. While the new surface-brightness profile agrees very well with the Trager profile over the region they share in common, it is preferable to use the *HST*/ACS profile to determine the core radius for several reasons: in particular, we have star counts for the new data which allow for determining the Poisson uncertainties associated with the profile; and the new profile is native to the F606W bandpass, removing any potential errors in the conversion from V to F606W. Since both profiles agree well, the derived core radius would not change significantly if only the old data were used. The comparison between the model and the data is shown in Figure 5. As noted is Section 3.1, these values are appropriate for $\sim 0.8\ M_{\odot}$ stars.

Combining these constraints with the luminosity function from the reference annulus, we have used the dynamical model to predict how the luminosity function changes as a function of radius. Figure 4 compares those predictions against the measured luminosity functions in annuli at larger radii. There are disagreements at the 10%–15% level in the numbers of subgiant and giant branch stars predicted, but the agreement is good along the main sequence. As expected, the relative contribution of lower luminosity, lower-mass main-sequence stars increases with increasing radius. The global luminosity function is derived by integrating the model over its full extent out to the tidal radius. That integration shows that, while the ACS/WFC data cover only a small fraction of the cluster area, half of the cluster members lie within this observed region.

3.3. The MLR and Global Mass Function

Transforming a luminosity function to a mass function requires an MLR. While empirical data, based on stellar binaries, can be used to derive this relationship for disk dwarfs, no such data exist for metal-poor halo stars; consequently, we must rely on MLRs derived from theoretical models. Figure 6 compares the results from four sets of models, by Baraffe et al. (1997), Montalban et al. (2000), Pietrinferni et al. (2006), and the DSEP models from Dotter et al. (2007). We show comparisons in both the mass–luminosity plane and, where those data are available, in the mass–M_V plane. Only the DSEP and Pietrinferni et al. (2006) models are available in the F606W bandpass used in this study. All four MLRs are similar in shape, although there are small offsets at $\sim$10% level in the absolute calibrations. We take the recent DSEP calculations as the reference for the present analysis, although we will consider the effects of using different MLRs. It is important to note that the good agreement between the Pietrinferni et al. (2006) and DSEP models, and the differences between those models and older models, is undoubtedly related to improvements in the understanding of stellar physics in recent years. These improvements cover a wide range from inclusion of heavy element diffusion to improved reaction rates to a better understanding of low temperature and molecular opacities. It should therefore be no surprise that there are system-

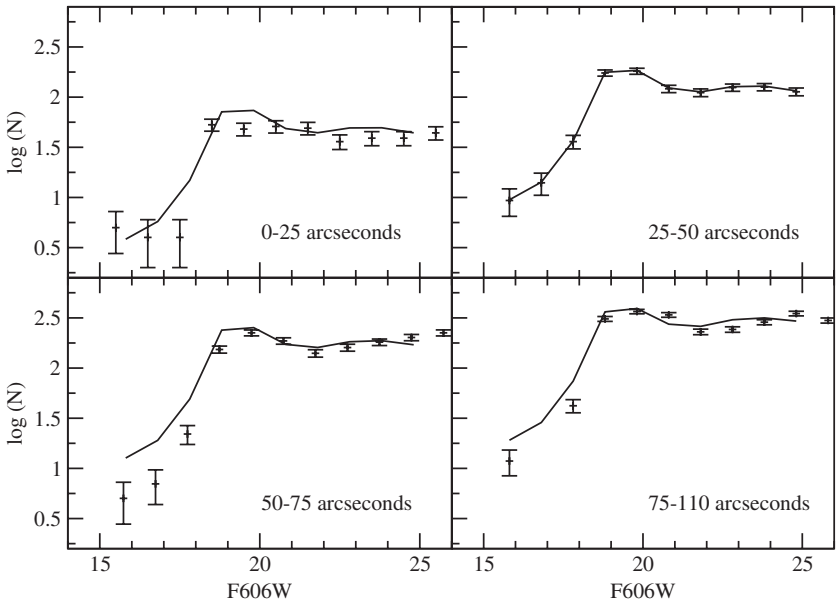

Figure 4. Observed luminosity functions from the center of the cluster to the edge of the ACS field of view compared to the luminosity functions from the King-model code. The 25″–50″ luminosity function is the input to the King-model code. The model and data are in good agreement, within the observational uncertainties, for main-sequence stars. The deficit of red giant branch stars in the 50″–75″ annulus appears to be real as the surface brightness also dips at that radius in Figure 5.

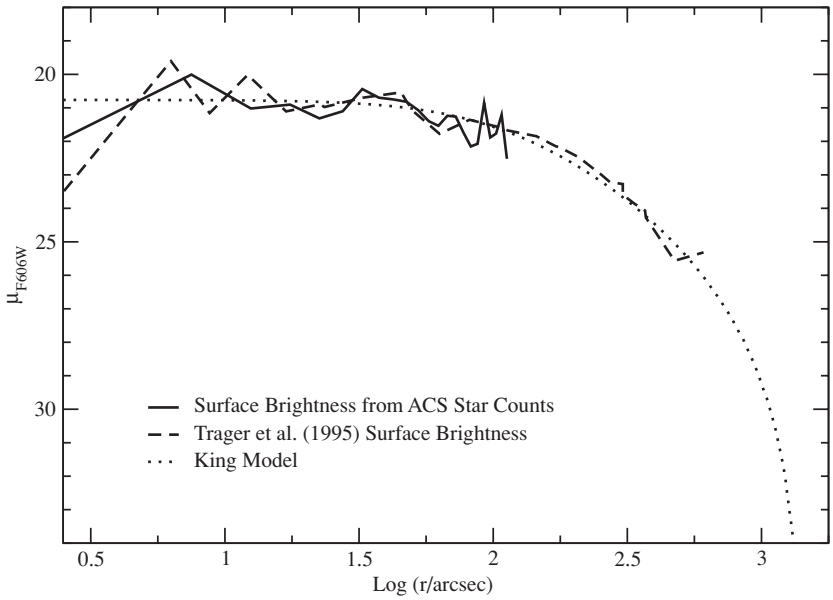

Figure 5. Surface-brightness profiles from the King-model code, our ACS star counts, and Trager et al. (1995) (converted to F606W magnitudes). Using a core radius of 1.′57 and a tidal radius of 24.′2 in the model results in very good agreement. The uncertainty in the observed surface brightnesses are related to the Poisson statistics of the red giant branch stars, this results in an uncertainty of approximately 10%.

atic disagreements between the older and newer sets of models. As our final mass functions are dependent on the derivatives of the MLR, we present these derivatives in Figure 7. In general all of the models change in the same manner with the more recent models, DSEP and Pietrinferni et al. (2006), agreeing extremely well. In particular, we note that the derivatives are smooth over the region from 0.5 to 0.8 $M_{\odot}$.

As mentioned in Section 3.1, we have used the MLR from the DSEP models to transform the global luminosity function to a mass function, determining the mass corresponding to the center of each luminosity bin. The bounding magnitudes on each bin were also converted to masses in order to find the mass range contained in each bin. The number of stars in each mass bin is divided by the width of the mass bin resulting in units of number of stars per unit mass. These data are listed in Table 1. For main-sequence stars, this technique works well. However, the bins in the luminosity function through the upper subgiant and red giant branch sample very small intervals in mass, leading to substantial uncertainties in the derived mass densities. Consequently, we have not included those stars in the derived mass function.

Figure 8 shows the global mass function for NGC 6366 together with the best-fit power law. While the power law is clearly not a good match to the data, it gives a means of comparing the mass function of NGC 6366 to other clusters. The results are notable in two respects. First, the power law has an index of $\alpha = 0.63$; that is, the number density of stars per unit mass decreases significantly with decreasing mass. Systematic uncer-

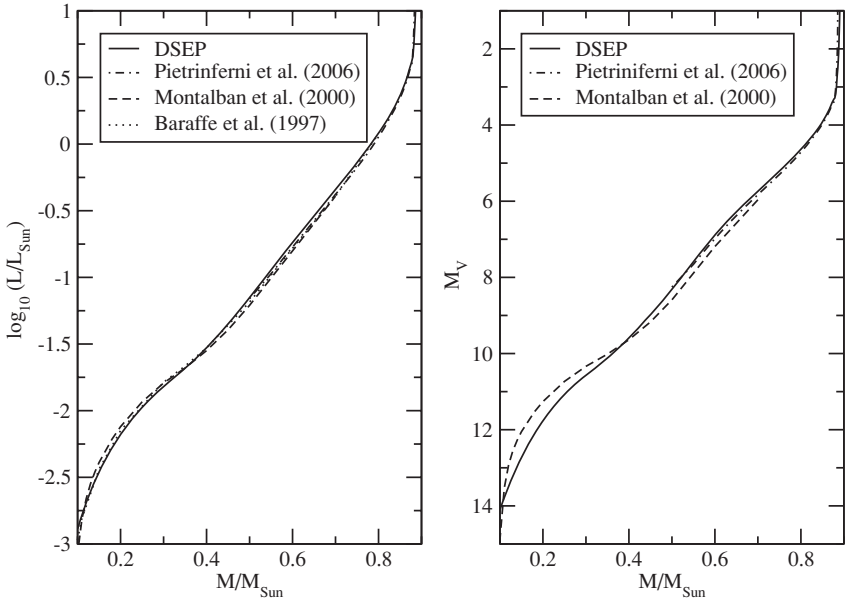

Figure 6. Mass–luminosity and mass–magnitude relations for the DSEP models used in this work compared to several models from the astronomical literature. The models all give very similar results, particularly in the $\sim$0.6 $M_{\odot}$ range where the global mass function dips.

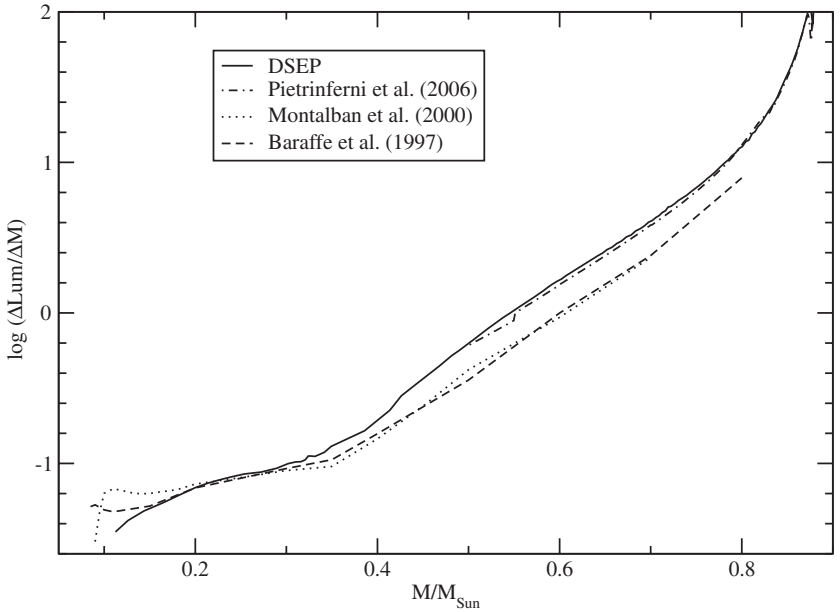

Figure 7. Derivatives of the MLR used in this work as well as several previously published models. All of the models predict very similar smooth behavior and the more recent models agree better than the older models.

tainties in isochrone fitting propagate to an uncertainty of $\pm$0.04 in the slope of the mass function and the uncertainties in the models are perhaps twice that, suggesting a total uncertainty in the mass function slope of $\sim \pm 0.1$. The slope is a sharp contrast to most other clusters, where $\alpha \sim -1$, but is comparable with other dynamically modified systems such as NGC 6218 ($\alpha \sim 0$, De Marchi et al. 2006), NGC 6712 ($\alpha \sim 0.9$, Andreuzzi et al. 2001), and NGC 2298 ($\alpha \sim 0.5$, De Marchi & Paresce 2007).

The second notable feature in Figure 8 is the significant deviations from the power-law fit. In particular, there is a sharp dip in number density between $\sim$0.7 and $\sim$0.5 $M_{\odot}$ (between -0.15 and -0.30 in $\log(M)$). This mass range corresponds to a magnitude range from $m_{\mathrm{F606W}} = 19.3$ to 22.3, approximately 0.5–1.5 mag below the MSTO.

Table 1
The Global Mass Function for NGC 6366

$M/M_{\odot}$	Completeness	$\log_{10}(N)$	$\log_{10}(N-\sigma)$	$\log_{10}(N+\sigma)$
0.821	0.996	4.891	4.802	4.965
0.797	1.000	4.795	4.757	4.830
0.738	0.999	4.658	4.623	4.690
0.657	0.997	4.523	4.481	4.560
0.578	0.995	4.582	4.539	4.622
0.504	0.988	4.653	4.611	4.691
0.424	0.977	4.662	4.621	4.699
0.328	0.957	4.536	4.492	4.577

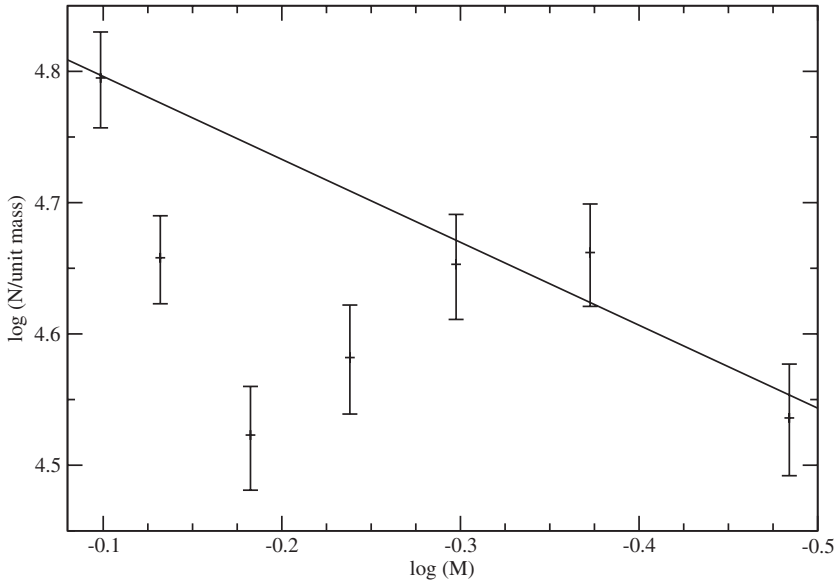

Figure 8. Global mass function for NGC 6366: for ease of comparison, the data are binned to match the cluster luminosity function (Figures 4 and 10). The line is a power law of index 0.63 fit to the observations over main sequence and subgiant branch. The bin with the lowest mass has $m_{\rm F606W} = 25.25$ and the highest mass bin has $m_{\rm F606W} = 18.75$. Following the convention from the luminosity function, high-mass stars are on the left in this figure, while low-mass stars are on the right.

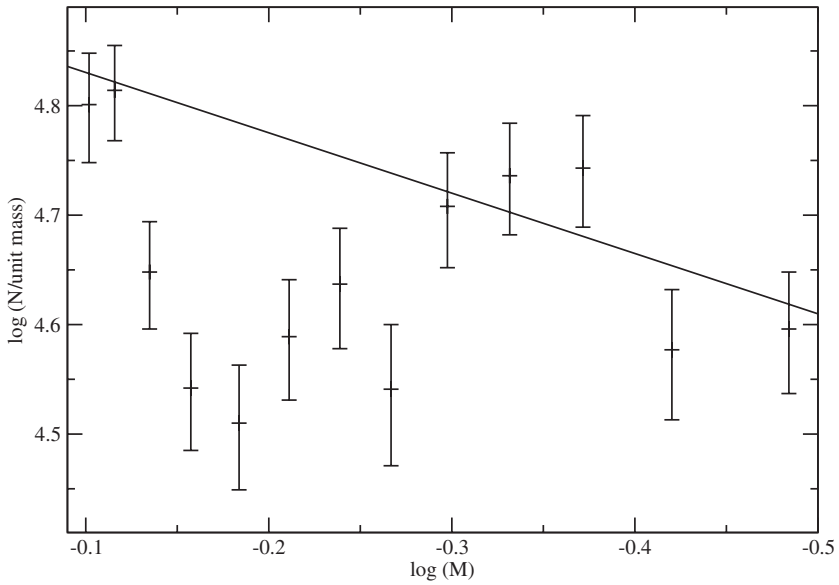

Figure 9. Global mass function constructed using bins half as wide as in Figure 8. The lowest bin in the dip is 6.7σ below the power-law fit.

Looking at Figure 8, there is a possibility that the dip in the mass function could be explained not by a lack of stars on the main sequence but, instead, could be caused by uncertainties in the cluster turnoff mass resulting in a surplus of stars at the MSTO. To examine this possibility, we have constructed a second global mass function with finer binning. This function can be seen in Figure 9. The finer binning allows for careful selection of main-sequence stars avoiding the evolved stars at the MSTO. The global mass function is fit with a power law over the mass range corresponding to F606W = 19–25.5 avoiding the bins in the dip (i.e. excluding $-0.15 > \log(M) > -0.27$). The MSTO is at approximately F606W = 18.5 corresponding to a mass of $0.827\ M_{\odot}$. The resulting power law has an index of $\alpha \sim 0.55$ suggesting that confusion with evolved stars was not an issue in the more coarsely grained mass function. The log–log nature of the mass function plots disguise the true significance of the dip. Indeed, the lowest point of the dip in the coarsely binned mass function is 4.7σ below the power law, while the lowest point of the finely binned mass function is 6.7σ lower than the power law. The dip becomes even more significant given that the deviation is correlated across multiple bins, each of which is many sigma below the fit. A second issue could artificially inflate the number of stars at the MSTO if the adopted distance modulus is incorrect, specifically if the cluster is assumed to be too distant. In this situation, the MLR is shifted and stars along the upper main sequence will be assigned the same mass as the turnoff stars, artificially enhancing the number of high-mass stars in the cluster. However, to have any effect on the mass function of NGC 6366, the distance modulus would have to be in error by over 0.25 mag, while the expected uncertainty in the distance modulus from the isochrone fitting in Figure 1 is approximately one quarter of that.

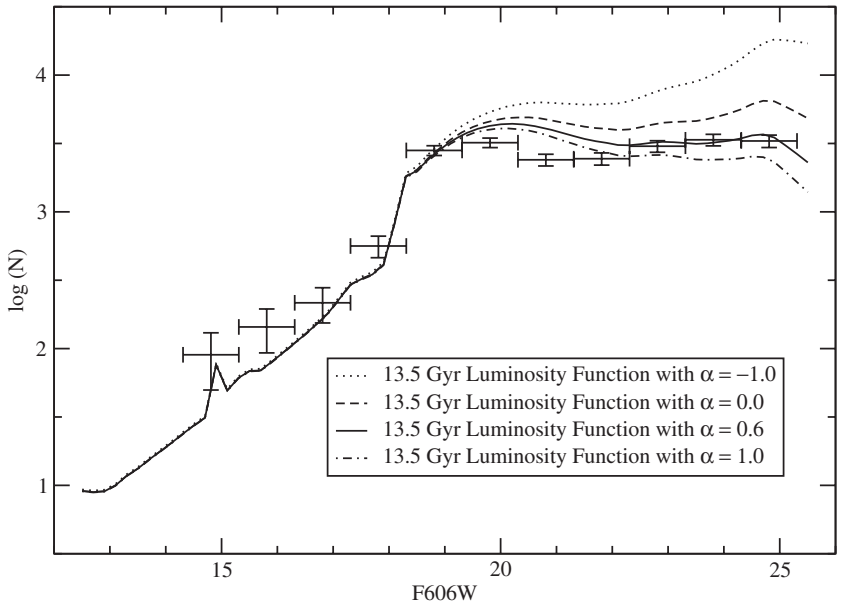

Figure 10. Global luminosity function of NGC 6366 with theoretical luminosity functions from DSEP. The horizontal lines on the observed luminosity function show the width of each luminosity bin. The theoretical luminosity functions are all based on the best-fitting isochrone from the CMD and have been generated with a range of power-law indices. The luminosity function with $\alpha = 0.6$ provides the closest match to the data, although there is a significant discrepancy in the magnitude range $20 < m_{\rm F606W} < 22$.

The missing stars can also be seen in a direct examination of the cluster luminosity function. Figure 10 shows the global luminosity function for NGC 6366 plotted with theoretical luminosity functions from DSEP with power-law indices of $\alpha = -1.0$, 0.0, 0.6, and 1.0. Of these, the only theoretical luminosity function which matches the observations at both the bright and faint ends is the one with $\alpha = 0.6$, in good agreement with the line fitted to the mass function in Figure 8. None of the other chosen indices match the observed cluster luminosity function over the extremes of the magnitude range and none of the theoretical luminosity functions are able to match the deficit of stars immediately below the MSTO. This serves as a check that the dip in the mass function is not an error introduced in the procedure generating the mass function, but is a real deficit of stars in that magnitude range. It is also important to note that the dip cannot be due to binary stars, the number of binaries in the mass range of the dip would have to be more than quadrupled compared to stars at higher and lower masses. If we assume that all stars lying between the $+3\sigma$ and $+6\sigma$ lines in Figure 2 are cluster binaries, then the additional stars provide only one quarter of the number of stars required to fill the dip. It is also not clear how binaries could preferentially be produced in the mass range of the dip.

The global mass function rests on the luminosity function in the reference annulus. Given that NGC 6366 is a sparse cluster, a possibility that needs to be considered is that the $\sim 0.6\,M_{\odot}$ dip stems from poor sampling statistics within that reference region. We can check this by computing the mass functions from the luminosity functions measured at other radii. Figure 11 shows the results, plotting local mass functions in the ACS field of view. All of the annuli except the innermost one show a deficit of stars around $0.6\,M_{\odot}$ when compared to a power-law mass function. The innermost annulus contains the fewest number of stars and therefore has the highest Poisson uncertainties. This adds further support to the claim that NGC 6366 is really missing stars in the middle of the mass range currently existing in the cluster.

One further check can be completed to investigate whether the dip in the global mass function is due to the region used as input to the dynamical models, the models can be run using the other three regions as input. The results of this modeling can be seen in Figure 12. All the annuli show a consistent pattern with a larger number of stars near the MSTO, a relatively smaller number of stars at $0.6\,M_{\odot}$ ($\log_{10}(M) = -0.22$), and then an increase lower on the main sequence until the final drop at the adopted magnitude limit. The index of the power laws steepen from $\alpha = 0.75$ in the outer annulus to $\alpha = 1.96$ in the cluster core, in line with expectations of mass segregation. As shown by the results from Figure 9, this result cannot be attributed to uncertainties in the exact turnoff mass.

4. DISCUSSION

Mass segregation and tidal stripping are predicted to combine to preferentially remove low-mass stars from stellar clusters. As a cluster undergoes dynamical relaxation, energy equipartition leads to a correlation between velocity dispersion and mass. High-mass stars have lower velocity dispersions, and tend to be confined to the central regions, while low-mass stars populate the outer regions of the cluster. As a result, those lower-mass stars are more vulnerable to being stripped from the cluster through gravitational interactions with other massive bodies.

The consequences of this type of dynamical evolution are clearly evident in many Galactic open clusters, including the Hyades, NGC 2516, and Praesepe, and are also likely to account for the flatter mass functions exhibited by several other bulge GCs. Lying in the inner Galaxy, NGC 6366 is likely subject to frequent gravitational encounters, which could lead to the severe depletion of low-mass stars evident in Figure 8. The work of Gnedin & Ostriker (1997) predicts a very short lifetime for NGC 6366 of between 0.12 and 0.61 Hubble times suggesting that stripping and tidal shocks play a very important role in this cluster. Thus, the steep positive slope to the mass function is interesting, but is not a huge surprise.

However, the theoretical expectation is that both mass segregation and the consequent tidal stripping should be a smooth function of mass, with stellar depletion increasing with

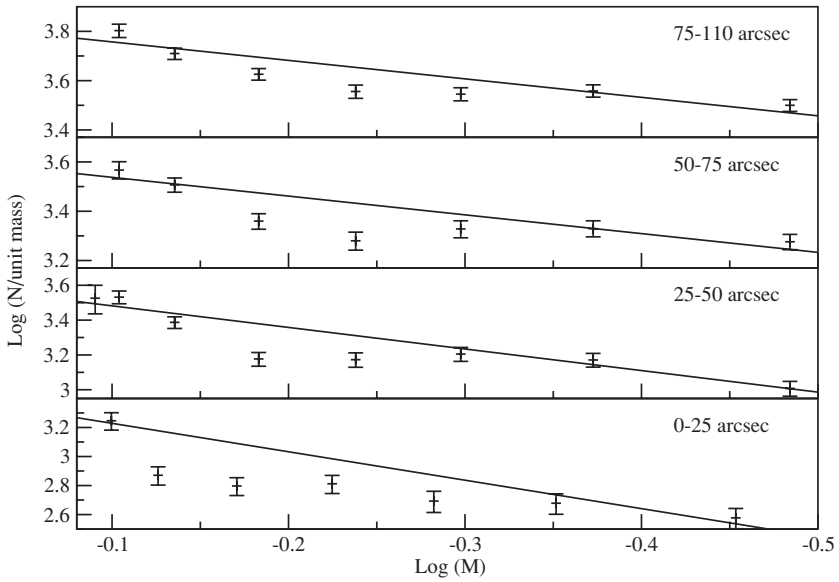

Figure 11. Local mass functions for annuli inside the ACS field of view. The solid lines are power-laws fit to the data excluding the dip. All the annuli show a deficit of stars near $\log_{10}(M) = -0.2$. The power-laws fit to the local mass functions have indices of 0.75, 0.76, 1.24, and 1.96 for the 75″–110″, 50″–75″, 25″–50″, and 0″–25″ annuli, respectively.

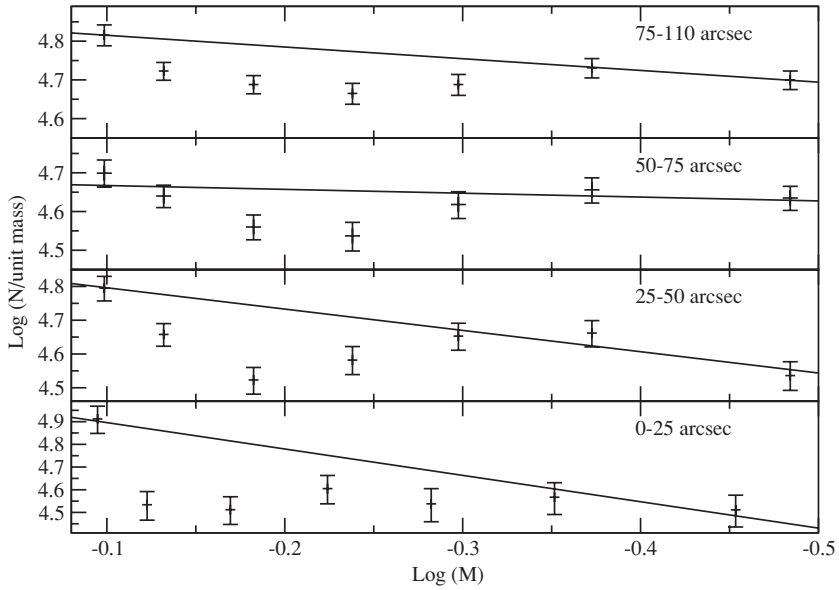

Figure 12. Global mass functions similar to Figure 8 using all four regions as inputs into the dynamical models. The lines are labeled with the annulus used as input to the models. All of the annuli show a deficit of stars around 0.6 $M_\odot$ ($\log_{10}(M) = -0.22$). The MSTO is at 0.8 $M_\odot$ ($\log_{10}(M) = -0.1$). The spacing of points in this figure corresponds to 1 mag bins in the luminosity function.

decreasing mass. Thus, for a system with a power-law IMF, one might expect α to increase smoothly with time. It is difficult to envisage how this process could lead to preferential depletion of $\sim$0.6 $M_\odot$ stars. The lack of stars in this mass range cannot be explained by the MLR used. Filling this depression would require a large kink in the MLR, which is not seen in any theoretical models of lower main-sequence metal-poor stars. Selecting a different theoretical MLR from those shown in Figure 6 will not affect the shape of the mass function. As noted above, the Pietrinferni et al. (2006) models are essentially identical to the DSEP models. The older models can disagree by $\sim$10%; however, the MLRs are smooth within the key mass range of interest here, so while the location of the dip may change by as much as 0.05 $M_\odot$, the shape of the mass function will not.

Clearly, additional observations are required to further investigate this interesting cluster. In particular, proper motions would allow a determination of the space motion, and hence an estimate of the Galactic orbit and the potential for past dynamical interactions. The present observations include approximately half the cluster members, yet it remains possible that our mass function analysis is affected by sampling uncertainties within this rather sparse cluster. Further wide-field imaging, covering the full cluster, will provide insight into whether the $\sim$0.6 $M_\odot$ deficit apparent in our data set is really a global property of the cluster. Finally, detailed spectroscopy of giant branch and horizontal branch stars will provide important information on whether there are any abundance anomalies associated with the unusual cluster mass function.

We are currently in the process of analyzing data for the remaining 64 Galactic GCs in the ACS Survey, including a significant number of clusters in the Galactic bulge. Those data will allow us to place the NGC 6366 mass function in a broader context.

Support for program GO-10775 was provided by NASA through a grant from the Space Telescope Science Institute, which is operated by the Association of Universities for Research in Astronomy, Inc., under NASA contract NAS 5-26555. A.A., A.M., and A.R. are funded by the Instituto de Astrofisica de Canarias (grant P3-94) and by the Ministry of Education and Science of the Kingdom of Spain (grant AYA-2008-67913). The authors would like to thank I. King for reading the manuscript and making several useful suggestions.

REFERENCES

Alonso, A., Salaris, M., Martínez-Roger, C., Straniero, O., & Arribas, S. 1997, A&A, 323, 374
Anderson, J. 1997, PhD thesis, Univ. of California, Berkeley
Anderson, J., & King, I. R. 2006, (ACS ISR 2006-01) (Baltimore, MD: STScI)
Anderson, J., et al. 2008, AJ, 135, 2055
Andreuzzi, G., De Marchi, G., Ferraro, F. R., Paresce, F., Pulone, L., & Buonanno, R. 2001, A&A, 372, 851
Baraffe, I., Chabrier, G., Allard, F., & Hauschildt, P. H. 1997, A&A, 327, 1054
Bedin, L. R., Anderson, J., King, I. R., & Piotto, G. 2001, ApJ, 560, L75
Bedin, L. R., Cassisi, S., Castelli, F., Piotto, G., Anderson, J., Salaris, M., Momany, Y., & Pietrinferni, A. 2005, MNRAS, 357, 1038
Carretta, E., & Gratton, R. G. 1997, A&AS, 121, 95
Cool, A. M., Piotto, G., & King, I. R. 1996, ApJ, 468, 655
Da Costa, G. S. 1982, AJ, 87, 990
De Angeli, F., Piotto, G., Cassisi, S., Busso, G., Recio-Blanco, A., Salaris, M., Aparicio, A., & Rosenberg, A. 2005, AJ, 130, 116
De Marchi, G., Leibundgut, B., Paresce, F., & Pulone, L. 1999, A&A, 343, 9L
De Marchi, G., & Pulone, L. 2007, A&A, 467, 107
De Marchi, G., & Paresce, F. 1994, ApJ, 422, 597
De Marchi, G., & Paresce, F. 1995, A&A, 304, 211
De Marchi, G., & Pulone, L. 2007, A&A, 467, 115
De Marchi, G., Pulone, L., & Paresce, F. 2006, A&A, 449, 161
Dotter, A., Chaboyer, B., Ferguson, J. W., Lee, H., Worthey, G., Jevremović, D., & Baron, E. 2007, ApJ, 666, 403
Gnedin, O. Y., & Ostriker, J. P. 1997, ApJ, 474, 223
Gunn, J. E., & Griffin, R. F. 1979, AJ, 84, 752
Harris, H. C. 1993, AJ, 106, 604
Harris, H. C. 1996, AJ, 112, 1487
Harris, W. E., et al. 1997, AJ, 114, 1030
King, I. R., Anderson, J., Cool, A. M., & Piotto, G. 1998, ApJ, 492, L37
King, I. R., Sosin, C., & Cool, A. M. 1995, ApJ, 452, L33
Koch, A., Grebel, E., Odenkirchen, M., Martinez-Delgado, D., & Caldwell, J. 2004, AJ, 128, 2274
Montalban, J., D'Antona, F., & Mazzitelli, I. 2000, A&A, 360, 935
Oort, J. H., & van Herk, G. 1959, Bull. Astron. Inst. Netherlands, 14, 299
Paresce, F., & De Marchi, G. 2000, ApJ, 534, 870
Paresce, F., De Marchi, G., & Jedrzejewski, R. 1995, ApJ, 442, 57
Paust, N. E. Q., Chaboyer, B., & Sarajedini, A. 2007, AJ, 133, 278
Pietrinferni, A., Cassisi, S., Salaris, M., & Castelli, F. 2006, ApJ, 642, 797
Pike, C. D. 1976, MNRAS, 177, 257
Piotto, G., & Zoccali, M. 1999, A&A, 345, 485
Piotto, G., et al. 2002, A&A, 391, 945
Reid, I. N., Kirkpatrick, J. D., Liebert, J., Gizis, J. E., Dahn, C. C., & Monet, D. G. 2002, AJ, 124, 519
Richer, H. B., et al. 1997, ApJ, 484, 741
Richer, H. B., et al. 2002, ApJ, 574, L151
Richer, H. B., et al. 2008, AJ, 135, 2141
Rosenberg, A., Aparicio, A., Saviane, I., & Piotto, G. 2000, A&AS, 145, 451
Salaris, M., Chieffi, A., & Straniero, O. 1993, ApJ, 414, 580
Sandage, A. R. 1954, AJ, 59, 162
Sarajedini, A., et al. 2007, AJ, 133, 1658
Sirianni, M., et al. 2005, PASP, 117, 1049
Spitzer, L. 1987, Dynamical Evolution of Globular Clusters (Princeton, NJ: Princeton Univ. Press)
Tayler, R. J. 1954, AJ, 59, 413
Trager, S. C., King, I. R., & Djorgovski, S. 1995, AJ, 109, 218
Zinn, R. 1985, ApJS, 55, 45
Zinn, R., & West, M. J. 1984, ApJS, 55, 45